Flow, Turbulence and Combustion (2026) 116:15
https://doi.org/10.1007/s10494-025-00712-0

RESEARCH

Direct, large eddy, and Reynolds-averaged Navier-Stokes simulations of hydrogen periodic planar jets in argon

Diego A. Quan Reyes[1] · Nick Diepstraten[1] · Alessandro Ballatore[1] · Dirk Roekaerts[2] · Jeroen van Oijen[1]

Received: 11 March 2025 / Accepted: 22 September 2025

Abstract

The development of a hydrogen jet injected into quiescent argon was investigated in a temporal jet configuration via direct numerical simulations (DNS). A case of argon mixing in argon was used as the basis for comparison. Both systems were computed at jet Reynolds numbers of 5000 and 10,000. Attention was focused on the mechanism driving the mixing process, as well as the turbulent momentum and scalar transport. The physical properties of argon are very different from those of hydrogen (density ratio (≈20), kinematic viscosity ratio (≈0.1), and Lewis number ratio (≈ 3)), leading to significant differences between the two cases, in jet structure, instantaneous and mean profile characteristics. A common feature in all systems was the emergence of large quasi-two-dimensional rotating structures, responsible for the engulfment of surrounding fluid, which created elongated regions where most molecular mixing takes place, with one difference being faster mixing in the hydrogen cases. An a priori assessment of the classical gradient hypothesis for turbulent fluxes revealed that the turbulent Schmidt number (Sc_t) and C_μ are not constant in space nor time, with local values ranging from $0.2 - 1.4$, and $0.6 - 1.1$, respectively, contrasting with the constant values used in Reynolds-Averaged Navier-Stokes (RANS) modeling. Additionally, an evaluation of a two equation RANS model and a dynamic one-equation large eddy simulations (LES) model was made *a posteriori* by comparison of their predictions with the DNS results. Both approaches exhibited significant deviations from the DNS, primarily at the early stage, but relaxed to similar solutions as time progressed. The properties at the jet edge were less well predicted by the RANS model than by the LES model. This is attributed to both gradient diffusion modeling and the impact of a turbulent/non-turbulent interface. Possible model enhancements are discussed.

Extended author information available on the last page of the article

Published online: 08 December 2025

Graphical Abstract

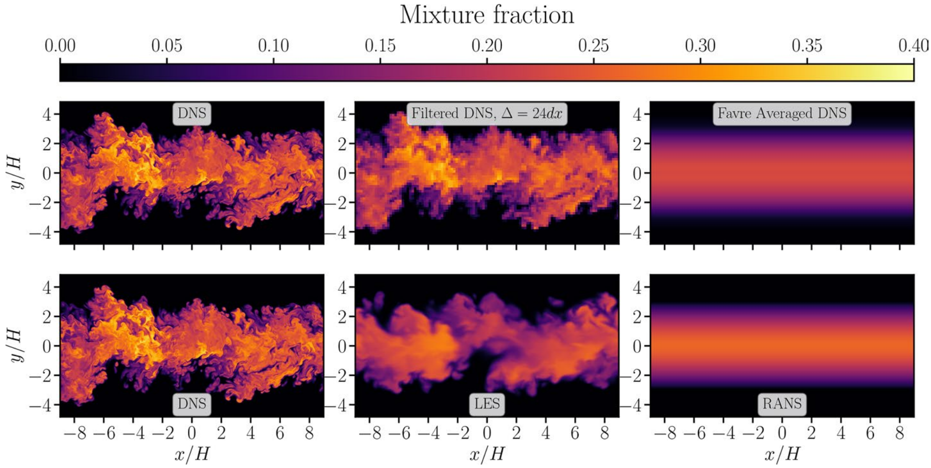

Keywords Hydrogen · DNS · LES · RANS · Turbulence

1 Introduction

Hydrogen can play an essential role as an energy carrier in power generation and industrial energy use, contributing to reversal of the trends of carbon emissions into the atmosphere and the resulting human-induced climate change. One of the open questions of a hydrogen-based economy is how to convert clean hydrogen back into useful power and energy. The Argon Power Cycle (APC) that seeks to use argon as the working fluid, appears to be an interesting combustion cycle candidate due to its higher specific heat ratio compared to air, resulting in an increased cycle efficiency. When used with clean hydrogen and oxygen, the APC would be free of CO_2 and nitrogen oxides.

The development of APC and related systems requires reliable turbulence models for mixing and combustion dynamics. These models are needed because the highly turbulent flows involved cannot be fully resolved via direct numerical simulations (DNS). For example, the Reynolds number (Re) of a hydrogen jet in an internal combustion engine can reach values $Re > 10^6$, and the number of grid points needed to resolve turbulent flow scales as $\mathcal{O}(Re^{9/4})$ (Nieuwstadt et al. 2016; Pope 2005). Statistical methods, Reynolds-averaged Navier-Stokes (RANS) or Large Eddy Simulations (LES), rely on closure assumptions empirically validated for canonical flows. Applications of these closure models to other flows must be made with care (Spalding 1975), especially considering that the physical properties of hydrogen are very different from those of the fluids used to develop such closures (Jones and Launder 1972).

This study has three main objectives: first, to understand the momentum and scalar transport of a turbulent hydrogen jet in quiescent argon. Second, to evaluate the classical gradient hypotheses for momentum and scalar transport. Lastly, to evaluate the accuracy of coarse-scale methods (RANS and LES) and suggest improvements.

For computational efficiency reasons, the jet is not studied as a spatially developing jet but as a temporally developing jet, a configuration with periodic boundary conditions in the jet's streamwise direction. A DNS of a temporally developing planar jet of hydrogen surrounded by argon is computed, and contrasted against a homogeneous case (argon in argon). In this way, the impact of differences in physical properties can be assessed. Both cases are computed at $Re = 5000$ and 10,000. These four cases are also computed using RANS and LES.

The value of $Re = 10{,}000$ was chosen as it was proposed analytically and supported by several experiments, that flows with $Re \approx 10^4$ will exhibit all the features of turbulent mixing and will not show qualitative changes with increasing *Re* (Dimotakis 2000). Consistent findings for round jets were reported in (Hill 1972): entrainment and turbulent fluctuations (responsible for turbulent transport) become independent of *Re* at values greater than 7000. These findings have been further confirmed in (Pitts 1991) and (Viggiano et al. 2018). RANS models and LES models initially formulated for high flow *Re*, need extensions or modifications for low *Re*. Here, these methods are validated both at $Re = 10{,}000$ and $Re = 5000$. Furthermore, the models have been validated first for equal density, constant viscosity and, near unity values of Schmidt and Prandtl number, and extensions are needed to handle deviations from these conditions. The mixing of $\mathrm{H_2}$ with Ar results in a situation with large property differences. For example, at standard conditions, Ar and $\mathrm{H_2}$ have a density ratio of $\rho_{\mathrm{Ar}}/\rho_{\mathrm{H_2}} \approx 20$, a kinematic viscosity ratio of $\nu_{\mathrm{Ar}}/\nu_{\mathrm{H_2}} \approx 0.1$, and a Lewis number ratio of $Le_{\mathrm{Ar}}/Le_{\mathrm{H_2}} \approx 3$. This is a type of system for which DNS have not been made before, and obtaining and analysing such results is the first challenge. Performing the DNS also give the opportunity to use it for validation of RANS and LES models. This can be done in an a priori way by testing whether closure assumptions in RANS or LES are satisfied by DNS solutions, and in an a posteriori way by testing whether relevant statistical moments predicted by RANS and LES agree with the value of these moments computed from the DNS fields. Doing these validations is the second challenge.

An essential prerequisite to obtain reliable results is the careful selection of numerical solution methods of the equations used in the different approaches. While the requirements are relatively easy to define in DNS and in RANS, in LES the situation is more complex, since the LES model assumptions and the numerical schemes both contribute error in the quantities to be evaluated. Furthermore, the precise meaning of comparison of LES and DNS has to take into account that LES by nature is a statistical approach (Pope 2004). Different categories of LES models have been developed, each with their advantages and limitations. For example, Vreman et al. (Vreman et al. 1997), for a weakly compressible temporal mixing layer, compared the performance of different subgrid models, comparing LES results with filtered DNS results. They found that the dynamic models generate better results than the non-dynamic models. An in-depth review from the perspective of a priori statistical characteristics of LES models and the important role played by discrete numerical operators, is presented by Moser et al. (Moser et al. 2021). Our results are obtained using a widely used dynamic one-equation model, described in Sect. 5.

To complete this introduction, we list in chronological order some previous studies that inspired the analysis of the present work. They concern different mixing configurations: mixing layer developing in space (sheared or shear free), temporal mixing layer, plane or round jet, etc. , but also differ according to which variables are different between the two streams that are mixed: density, viscosity, and/or scalar diffusivity. Each of these covers only part of the challenges addressed in this work. Knaepen et al. (Knaepen et al. 2004) performed a DNS vs LES comparison of a shear-free mixing layer and showed the ability of eddy viscosity models to capture the energy profile and turbulent fluctuations. Foysi and Sarkar (Foysi and Sarkar 2010) investigated compressible temporal mixing layers with *Re* up to 2×10^4, and with Mach numbers ranging from 0.3 to 1.2. They employed a form of approximate deconvolution together with a dynamic Smagorinsky subgrid model. Taquelmimt et al. (Taguelmimt et al. 2016) studied the effects of viscosity variations in temporal mixing layers and found a faster growth of turbulence in a higher viscosity ratio. Almagro et al. (Almagro et al. 2017) made a DNS study of low-speed turbulent mixing layers for density ratios 1,2,4 and 8. The growth rate of the mixing layer was found to decrease with increasing density ratio, while the position of the mixing layer was shifting in the direction of the low density stream. Gauding et al. (Gauding et al. 2021) made a DNS study of temporal mixing layer between turbulent and non-turbulent flow with focus on the scaling of structure functions of scalar mixing. Huang et al. (Huang et al. 2021) performed LES of variable density mixing layers, developing from laminar initial conditions, and found how the development of streamwise structures is influenced by density ratio. Salizzoni et al. (Salizzoni et al. 2023, 2024) reported detailed analytical and numerical studies on the influence of density ratio on the entrainment coefficient of jets.

The understanding and modeling of a hydrogen jet mixing in an argon environment poses challenges that go beyond those addressed in the mentioned studies, because of the combined effects of differences in density, viscosity and Lewis number. There is a need for a detailed study of the phenomena and the ability of RANS and LES models to describe turbulent mixing accurately. The rest of this work is structured as follows. In Sect. 2 the theoretical background of this study is presented. In Sect. 3, the setup of the numerical experiment is introduced. In Sect. 4, a phenomenological analysis of instantaneous fields is performed, revealing the nature of the flow evolution for all DNS cases. Section 5 presents an a priori assessment of the gradient hypothesis. In Sect. 6, RANS and LES are evaluated against the DNS. Conclusions are given in Sect. 7.

2 Theory and modeling

2.1 Governing equations

The principles that govern the dynamics of fluids are the conservation of mass, momentum, and energy. When multiple chemical species are present, an extra conservation equation is needed. Introducing the density ρ, velocity u, temperature T, pressure p, stress tensor τ, specific isochoric heat capacity c_v, specific isobaric heat capacity c_p, thermal conductivity λ, dynamic viscosity μ, enthalpy h, specific gas constant $\mathcal{R} = R_u/M$, with M the mixture mean molar mass, species mass fractions Y_α, time t and spatial Cartesian coordinates x_1, x_2, x_3, and taking into account that in the case of mixing between two uniform streams only one species mass fraction has to be computed, these principles can be written in differential form as:

Mass conservation

$$\frac{\partial \rho}{\partial t} + \frac{\partial}{\partial x_i}(\rho u_i) = 0, \quad i = 1, 2, 3. \tag{1}$$

Momentum conservation

$$\rho \frac{\partial u_j}{\partial t} + \rho u_i \frac{\partial u_j}{\partial x_i} = -\frac{\partial p}{\partial x_j} + \frac{\partial \tau_{ij}}{\partial x_i}, \quad j = 1, 2, 3. \tag{2}$$

Energy conservation

$$\begin{aligned}\rho c_v \frac{\partial T}{\partial t} + \rho c_v u_i \frac{\partial T}{\partial x_i} = \frac{\partial}{\partial x_i}\left(\lambda \frac{\partial T}{\partial x_i}\right) - p\frac{\partial u_i}{\partial x_i} + \tau_{ij}\frac{\partial u_i}{\partial x_j} \\ + \frac{\partial}{\partial x_i}\left(h' \frac{\lambda}{Lec_p}\frac{\partial Y}{\partial x_i}\right) \\ - (h' - R'T)\left[\frac{\partial}{\partial x_i}\left(\frac{\lambda}{Lec_p}\frac{\partial Y}{\partial x_i}\right)\right].\end{aligned} \tag{3}$$

Species mass conservation

$$\rho \frac{\partial Y}{\partial t} + \rho u_i \frac{\partial Y}{\partial x_i} = \frac{\partial}{\partial x_i}\left(\frac{\lambda}{Lec_p}\frac{\partial Y}{\partial x_i}\right). \tag{4}$$

In Eq.(3) and (4) Y denotes the jet chemical species which is assumed to have a constant Lewis number Le (not necessarily unity), and Soret diffusion is neglected. Note that Eq. (4) neglects molecular weight gradients, and it may be unrealistic for hydrogen in argon due to the large molecular weight difference, this neglect would result in an over-prediction of molecular diffusion (Pitsch and Peters 1998). Despite the limitation, this simplification is the one used in virtually all commercial and open-source computational fluid dynamics codes, and thus it is employed here. Furhtermore, it is often assumed that molecular diffusion effects decrease with increasing turbulence, the validity of that assumption for hydrogen mixing in a heavier gas deserves attention in its own, and will be studied subsequently. In the previous two equations, the mass fraction of the ambient gas is $1 - Y$. This implies that the diffusion fluxes of the bath gas (Ar) balance the diffusion fluxes of the jet chemical species. In that way, the $h^{'}$ is introduced as $h' = h_{\text{jet}} - h_{\text{Ar}}$, and similarly for $R^{'}$. It is assumed that the flow exhibits ideal gas behavior i.e.:

$$p = \rho \mathcal{R} T \sum_{\alpha=1}^{2} Y_\alpha / M_\alpha. \tag{5}$$

Here α is the species index and M_α is the species molar mass. The fluid is assumed Newtonian, with vanishing bulk viscosity. Then the viscous stress tensor τ_{ij} is:

$$\tau_{ij} = \mu \left(\frac{\partial u_i}{\partial x_j} + \frac{\partial u_j}{\partial x_i} - \frac{2}{3}\delta_{ij}\frac{\partial u_k}{\partial x_k} \right). \tag{6}$$

In the reminder of this document, $x_1, x_2, x_3, u_1, u_2, u_3$ will be referred to as x, y, z, u, v, w, respectively.

2.2 Statistical modeling

If Eqs. (1)-(4) are integrated directly as in DNS, all flow scales are resolved and details of the flow are revealed, many of which are inaccessible via experiments. This enables the direct observation of phenomena without relying on statistics, but the computational cost becomes a bottleneck. The current state of the art allows the computation of cases with typical values of $Re \approx 10^4$. On the other hand, in statistical approaches, both LES and RANS, the physical variables are decomposed in mean and fluctuation and only a set of lower statistical moments is computed, implying the need for closure models. In RANS the averaging procedure is ensemble averaging over all fluctuations, in LES with spatial filtering it is spatial averaging over scales smaller than the filter width (sub-filter scale (SFS) fluctuations, or when the filter width comes from the grid size: sub-grid scale (SGS) fluctuations). Following common practice, we consider transport equations for density weighted (Favre) quantities. For any quantity Q we denote its average by $\bar{Q}$, and its Favre average by $\tilde{Q}$ and the fluctuation relative to the Favre average by $Q^{'}$, such that $Q = \tilde{Q} + Q'$. For example, averaging Eq. (2), neglecting viscous effects and assuming statistically homogeneous flow in y-direction (vanishing derivatives in the x and z-directions) results in:

$$\frac{\partial}{\partial t}(\bar{\rho}\tilde{u}) + \frac{\partial}{\partial y}(\bar{\rho}\tilde{v}\tilde{u}) + \frac{\partial}{\partial y}(\bar{\rho}\widetilde{u'v'}) = 0, \tag{7}$$

The last term of the equation represents the momentum transport by turbulent fluctuations (RANS) or subgrid fluctuations (LES), and for solving the equation a closure model is required.

In this study, we are not aiming at using the best possible RANS and LES models for the case studied but rather do a new validation study of widely used representative models: for RANS a two-equation eddy viscosity turbulence model for turbulent momentum transport and for LES a dynamic one-equation SGS viscosity model, in both cases combined with a gradient diffusion closure for turbulent scalar transport. We focus on the key concepts underlying the approaches, going back to early work on turbulent transport.

RANS' linear eddy viscosity models have in common that the transport of momentum and any scalar ϕ is modeled as (Gatski et al. 2002):

$$\bar{\rho}\widetilde{u_i'u_j'} = -\mu_t \frac{\partial \tilde{u}_i}{\partial x_j}, \tag{8}$$

$$\bar{\rho}\widetilde{\phi' u_j'} = -D_t \frac{\partial \tilde{\phi}}{\partial x_j}, \tag{9}$$

The turbulent viscosity (μ_t) and turbulent diffusivity (D_t) are assumed to be related by,

$$D_t = \frac{\mu_t}{\mathrm{Sc}_t}. \tag{10}$$

The turbulent Schmidt number (Sc_t) is commonly assumed to be constant having values around $0.7 - 0.9$ (for gases). However, actual values can vary by an order of magnitude, e.g., from 0.2 to 1.3 (Tominaga and Stathopoulos 2007). Turbulent viscosity μ_t can be estimated from the combination of turbulence length and time scales or in the context of k-ε models from the knowledge of the specific turbulent kinetic energy $\tilde{k}$ and its dissipation rate $\tilde{\varepsilon}$ (Pope 2005; Gatski et al. 2002).

$$\mu_t = \bar{\rho} c_\mu \frac{\tilde{k}^2}{\tilde{\varepsilon}}. \tag{11}$$

c_μ is an empirical constant with a typical value of 0.09. In k-ε RANS models, $\tilde{k}$ and $\tilde{\varepsilon}$ are obtained from model transport equations, but in DNS they can be obtained from their definition.

$$\tilde{k} = \frac{1}{2}\widetilde{u_i' u_i'}, \tag{12}$$

$$\tilde{\varepsilon} = 2\nu \widetilde{s_{ij} s_{ij}}, \tag{13}$$

$\nu = \mu/\rho$ is the kinematic viscosity of the mixture, and $s_{ij} = \frac{1}{2}\left(\frac{\partial u_i}{\partial x_j} + \frac{\partial u_j}{\partial x_i}\right)$ is the rate-of-strain tensor.

In LES SGS one-equation models, the SGS viscosity μ_{sgs} representing the influence of unresolved scales on resolved scales is modeled as $\mu_{sgs} = \bar{\rho} C_k \sqrt{k_{sgs}}\Delta$. With $C_k = 0.094$, Δ the filter width (mesh size), and k_{sgs} is solved from a model transport equation. The SGS turbulent Schmidt number is assumed constant.

The relative performance of RANS models, LES models and their hybrid forms have been widely studied. Most often, RANS has the main advantage of being computationally less costly, but the range of predicted phenomena and the generality of specific models is limited. For LES, more computational resources are needed, and a significant gain in accuracy and insight in transient phenomena is possible. However, validation of the assumptions made in RANS and LES described above remains crucial to obtain insight in the accuracy of their results. This is the goal of Sects. 5 and 6, respectively reporting on what DNS reveals about the accuracy of the gradient diffusion assumptions and how well the selected RANS and LES model results agree with the DNS results. The final discussion in Sect. 6.2 also briefly addresses the perspectives of possible model improvements compared to the selected models.

2.3 Models, numerical schemes, and implementation

Here we first summarize the models we used in DNS, LES and RANS and next discuss the numerical schemes.

2.3.1 Models

In DNS, the governing equations described in Sect. 2.1 are numerically solved. The viscosity of the mixture is calculated using the Davidson's momentum averaged mixing rules (Davidson 1993), this method show a maximum error of 2% with respect to the standard multi-component library of Ern and Giovangigli (Ern and Giovangigli 1995) on a binary mixing layer of pure H_2 and Ar. The thermal conductivity uses the rules by Mathur et al. (Mathur et al. 1967). Disco, the in-house DNS code employed here, has been in constant use and development for more than two decades. It has mainly been used for the study of reacting flow, with results published e.g. in [(Bastiaans et al. 2000, 2006; van Oijen 2011; Göktolga et al. 2015, 2021; Quan Reyes et al. 2024)].

The LES approach uses numerical filtering and includes SGS closure terms (Pope 2004). A dynamic k-equation model is used to obtain the SGS viscosity, which means that an additional transport equation is solved, providing the modeled subgrid specific turbulent kinetic energy k_{sgs} (Kim and Menon 1995). The SGS turbulent Schmidt number is set to $\mathrm{Sc}_t = 0.7$. The strengths and weaknesses of this approach in the representation of turbulence statistical properties are discussed by Moser et al. (Moser et al. 2021).

In RANS, the modeled ensemble averaged governing equations are solved. In this work the Renormalization Group (RNG) k-ε (Yakhot et al. 1992) is used. The simulations have been carried out using the commercial software package CONVERGE (Richards et al. 2021), with standard values for the model coefficients (Yakhot et al. 1992).

2.3.2 Implementation platform and numerical schemes

Table 1 lists the numerical schemes in the different approaches, as well as the computational cost and requirements for one of the cases at Re=10,000 that will be introduced later. For DNS, an in-house fully compressible solver named Disco was used. To resolve all scales to high accuracy DNS requires using high order schemes and a cell size $dx < 2\eta$, where η is the Kolmogorov length scale. Also of importance is that NSCBC boundary conditions are set to handle acoustic waves. In the initial phase of the simulation, acoustic waves form

Table 1 Overview of numerical schemes, parameters and requirements

Approach	DNS	LES	RANS
Software	Disco (in house)	OpenFOAM	CONVERGE
Diffusion	Compact finite difference, 6^{th} order (Lele 1992)	Linear 2^{th} order	Flux blending
Convection	de Lange 5^{th} order, (Lange 2007)	'cubicCorrected' scheme, 5^{th} order, not bounded	
Transient	Explicit Runge Kutta, 3^{rd} order	Implicit backward	Euler
Time Δt	$1 - 10 \times 10^{-9}$s	3×10^{-7}s adaptive	$< 10^{-7}$s adaptive
		4^{th} order	1^{st} order
CFL	<0.1	<1	<0.5
Cell edge length	$dx < 2\eta$; $5 - 13$m	$8dx$	dx
CPU-hours / Number of cores	$\mathcal{O}(10^5)$ hours, $10^3 - 10^4$ cores	$\mathcal{O}(10^3)$ hours, $\mathcal{O}(10^2)$ cores	1 hour, 1 core

when the pressure is adjusting to the hyperbolic profiles at the inlet. They exit the domain through the top and bottom subsonic outlet boundaries.

For LES, OpenFOAM was used. In LES, the quality of the model and the numerical method must be taken into account together (Pope 2004). Especially in ‘numerical LES’, as used here, when the filter size is set by the mesh size, and not an independent parameter. The numerical error made using a discrete representation of differential operators can have effects similar to those of the extra modeling terms representing the unresolved SGS phenomena. The ‘cubicCorrected’ scheme for the convection operator is the most accurate scheme available in OpenFOAM. Ballatore and van Oijen (Ballatore and Oijen 2024) in a study on hydrogen jets have shown that LES results obtained using the schemes used here agree well with experimental data. Care is taken to compute thermophysical properties with high accuracy. Instead of using the less accurate thermophysical properties available in OpenFOAM, they are computed externally using an in-house code named Chem1D, and looked up throughout the simulation. More information on the look-up procedure can be found in (Ballatore et al. 2025).

In RANS the requirements for the numerical schemes are less severe, especially when a fine grid is used. Since the flow studied in this work is statistically one-dimensional the RANS simulation can be made using a one-dimensional mesh, and it is affordable to use the same mesh size as used in DNS. Although much finer than required, it guarantees its accuracy.

3 Numerical experiment

A schematic of a periodic planar jet is depicted in Fig. 1. This system consists of two temporal mixing layers separated by a jet height H, with initial mean speed U, and periodic boundaries in the stream-wise direction. This configuration will exhibit a transition to turbulence. The simulation needs specification of an initial condition, also at the boundaries,

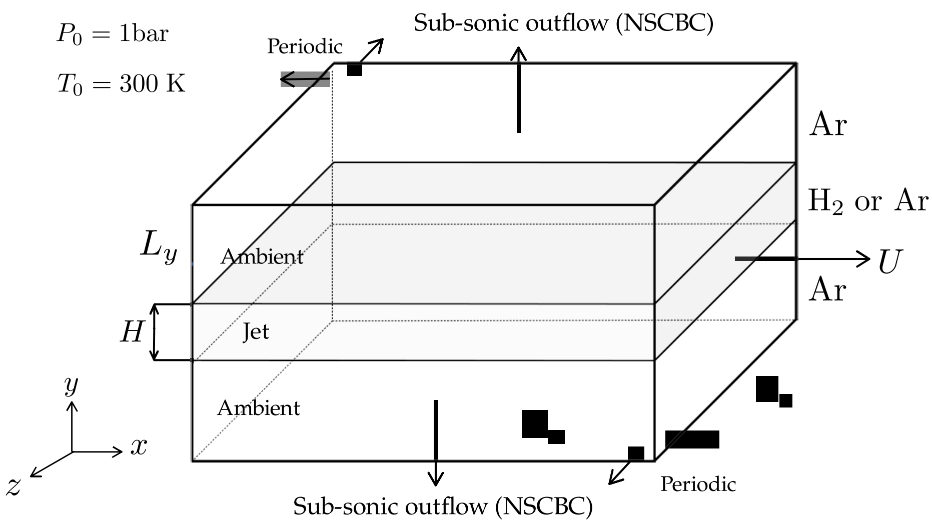

Fig. 1 Schematic of the planar jet

but is free of possible sensitivity to inflow boundary conditions after a short initial transient, in contrast with a continuous inflow of a jet issuing in ambient fluid (Boersma et al. 1998). The configuration has the advantage of being statistically one-dimensional. For this reason the averaging in the statistically homogeneous transverse directions can represent ensemble averaging as used in RANS. It is a canonical case that has sufficient similarity to injection of a fluid in a quiescent environment to be highly relevant. In the remainder of this work the term *jet* will be used to refer to a body of moving fluid, in its speed quality and not composition.

The computational domain is a box with volume $L_x \times L_y \times L_z$. The computational grid is uniform with equal cell size in all directions. For each of the four studied cases, the resolution was chosen to ensure that the Kolmogorov length-scale (η) is well resolved once the turbulence has developed i.e., $\mathrm{d}x/\eta < 2$ after 10 eddy turn-over times $(t_\mathrm{j} = U/H)$ (see Fig. 1 and Table 2).

Periodic boundaries are used for the x, z-faces. For the y-faces, the Navier-Stokes characteristic boundary conditions (NSCBC) (Poinsot and Lele 1992) are used in the form described in Ref. (Coussement et al. 2012), which includes important improvements compared to the original formulation, e.g., treatment for transverse terms with a relaxation factor as a function of the local Mach number (*Ma*). This allows acoustic waves to leave the domain and prevents reflections when the flow is non-orthogonal to the boundary, as reported in (Lodato 2011).

The jet velocity, species and temperature profiles for the mixing layers at the initial time are defined with a hyperbolic tangent function $f(y)$ that approximates a top-hat profile centered at the y plane with a thickness of δ_y i.e., $f(y) = \frac{1}{2} - \frac{1}{2}\tanh((|y| - \frac{1}{2}H)/\delta_y)$. Isotropic, divergence-free velocity fluctuations are superposed on this profile only in the jet region by filtering a random noise field. The resulting field is later scaled to have a root-mean-square value of 10% of U. Other studies on similar setups have used synthetic turbulence (Saad et al. 2017), with physical spectra e.g. (Comte-Bellot and Corrsin 1971), and showed no difference in the development of the turbulence compared to the filtered noise method used here. The only important parameter is the intensity of the filtered fluctuations.

Numerical values of all simulation parameters are presented in Table 2. The velocity and jet height were chosen to satisfy the condition that the jet time (or eddy turn-over time) is $t_\mathrm{j} = 3.5$ s. The results are reported as function of a dimensionless time $t^* = t/t_j$. All cases are initialized with a mean pressure 1 bar and temperature 300 K. All cases have a velocity U close to Ma=0.50, in order to have effects of compressibility.

The initial conditions of the DNS are also used as basis in LES and RANS, to be consistent. The LES initial fields are obtained using a box-filter of size $8dx$, which is the cell size used in LES. In Section 4, it will be shown that the smallest resolved scale in LES is in the energy cascading region. The RANS uses the same grid size as the DNS, implying that the solution is grid independent and not influenced by numerical dissipation. The RANS initial

Table 2 DNS parameters

Case	Le	Re	U [m/s]	H [m/s]	δ_y [mm]	L_x/H	L_y/H	L_z/H	$\mathrm{d}x_i$ [μm]	n_x	n_y	n_z
A5	1.0	5000	145	0.507	0.039	31.56	11.83	4.9	6.67	2400	901	375
A10	1.0	10,000	207	0.725	0.021	17.93	9.66	3.4	5.00	2600	1401	500
H5	0.27	5000	400	1.40	0.014	21.43	8.93	4.3	12.50	2400	1001	480
H10	0.27	10,000	565	2.00	0.155	17.00	8.00	3.5	10.00	3400	1601	700

fields are obtained from the DNS fields by density weighted spatial averaging of these fields in the *x*-*z*-plane, and hence are depending on *y* only.

4 Phenomenological analysis of the DNS solutions

By resolving all flow scales via DNS, the intricacies of the flow phenomena may be revealed. In this section we seek to understand the mechanisms by which momentum and scalar are transported. Thus, careful visualization of the flow is performed and the findings are contrasted with those reported in literature, with focus on the mixing of $\mathrm{H_2}$ in Ar.

The planar mixing layer (considered to be the simplest free shear flow, and yet not fully understood (Browand 1986)) is taking as starting point of the discussion. The periodic planar jet is closely related to it because it essentially consists of two mixing layers separated by a distance *H*. In (Browand 1986), Browand provided a comprehensive study on the nature of the mixing layer, starting from transition to turbulence, the mechanisms driving the mixing, and then to the remaining open questions. As that author explained, the shear drives the development of the mixing layer (in space or time, which can be related by a Galilean transformation); the most unstable waves will grow, creating thicker and stretched regions (as seen e.g., Fig. 2 from (Browand 1986)) forming large quasi-two-dimensional structures (vortices) that drive the mixing by entrainment of surrounding fluid. These vortices interact, preferentially in pairs. After the second to third vortex pairing takes place, the so-called *mixing transition* takes place, characterized by the appearance of the well-known $-5/3$ power law. The appearance of small-scale structures does not seem to affect the large quasi-two-dimensional vortices. Will these views hold for a $\mathrm{H_2}$ jet in Ar?

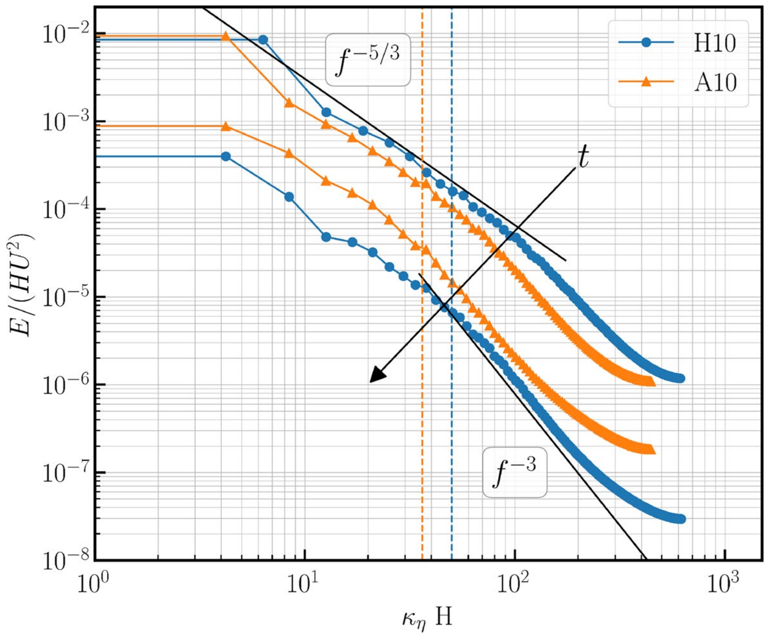

Fig. 2 Energy spectrum for cases H10 and A10 at $t^* = 10$ (top two lines) and $t^* = 50$ (bottom two lines). The vertical lines shows the smallest non-dimensional wave resolved in the les for each case

In Fig. 2, the energy spectrum (E) vs wave number *(κ)*, computed in a box of size H^3 located at the center of the jet for cases A10 and H10 at times $t^* = 10$ and 50 is shown. This figure demonstrates that the mixing transition has taken place and that both cases are sufficiently turbulent to exhibit the energy cascading process for $t^* > 10$. This figure also shows the maximum wavelength resolved in the LES. It is interesting to note that in case H10 the energy dissipates faster, this can be explained by the higher kinematic viscosity of H_2 compared to Ar.

From here, the notation Z will be used to denote the mass fraction of the jet species. In Fig. 3, the evolution of the scalar jet mass ($\rho Z/\rho_{\text{jet}}$), where ρ_{jet} is the initial density of the jet, in the middle *x*-*y* plane is shown. Three isocontours are given, corresponding to $\rho Z/\rho_{\text{jet}} = 0.01, 0.25, 0.50$, intended to provide a better description of the scalar distribution. First, we describe the main differences between the systems with homogeneous composition (A5 and A10), followed by the heterogeneous composition (H5 and H10). Cases A5 and A10 clearly show stronger wrinkling of the iso-contours and have a wider spread than cases H5 and H10, throughout the whole time range. As a consequence of this spreading, at $t^* \geq 30$, the iso-contour $\rho Z/\rho_{\text{jet}} = 0.50$ is absent. Next, contrasting case A5 and A10, shows that higher *Re* results in more wrinkling. This effect is stronger in the argon jet, since in A10, multiple 'islands' appear and persist throughout e.g., see the zoom of the area around $(x/H, y/H) = (6, 0)$ at $t^* = 40$, something not observed in H10, which may be due to the low *Le* of H_2 and will be investigated in a subsequent study. Two common features of all jets are: First, The presence of elongated flat regions of lower ρZ penetrating into the jet core. Examples of these regions can be found in A5 at $t^* = 10$ near $(x/H, y/H) = (4, 0.5)$ and H10 near $(x/H, y/H) = (5.5, 0.5)$ at $t^* = 40$. Second, the simultaneous growth in size

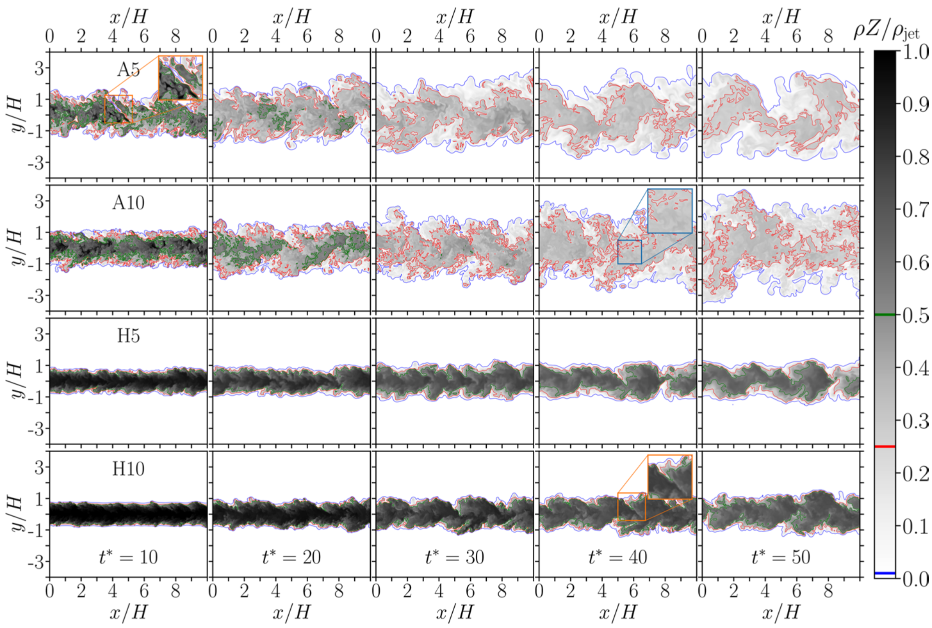

Fig. 3 Evolution of the scalar in the middle *z*-plane. From left to right, $t^* = 10, 20, 30, 40, 50$. From top to bottom: A5, A10, H5, and H10

of large-scale structures and decrease of the number of jet oscillations. This last feature is more prominent for homogeneous cases.

To better understand the difference in the spread rates observed qualitatively, the spreading of the Favre averaged momentum and scalar are analyzed. Introducing $y_{\tilde{Z}_{0.1}}$ and $y_{\tilde{u}_{0.1}}$ as the point along *y* where the mean momentum and mean scalar have reached 10% of the mean maximum. These read:

$$y_{\tilde{Z}_{0.1}}(t) = \ y \mid \bar{\rho}(t)\tilde{Z}(y,t)/\rho_{\mathrm{jet}} = 0.1 \times \max_y \left(\bar{\rho}(t)\tilde{Z}(y,t)/\rho_{\mathrm{jet}}\right), \tag{14}$$

$$y_{\tilde{u}_{0.1}}(t) = \ y \mid \bar{\rho}(t)\tilde{u}(y,t)/\rho_{\mathrm{jet}} = 0.1 \times \max_y \left(\bar{\rho}(t)\tilde{u}(y,t)/\rho_{\mathrm{jet}}\right). \tag{15}$$

Figure 4 depicts the growth of $y_{\tilde{Z}_{0.1}}$ and $y_{\tilde{u}_{0.1}}$, in time (spreading) and the ratio between cases with the same *Re*. From the left subfigure, it is clear that the Ar jets are spreading faster, both in terms of momentum and scalar. Another interesting aspect is the faster spreading of scalar over momentum. No clear trend is observed with respect to *Re*. In the right subfigure it can be seen that the influence of composition in spreading follows a behavior $(t^*)^{0.25}$ up to $t^* < 40$. For $t^* > 40$, all ratios tend towards a constant value, likely due to the homogenization of density by to mixing.

To understand the mechanisms driving the mixing, a more detailed visualization of instantaneous and averaged fields is presented. Figure 5 shows from top to bottom: (a) the instantaneous scalar field, (b) the mean scalar field obtained by Favre averaging in the *z*-direction, (c) the instantaneous momentum magnitude and (d) the Favre averaged scalar dissipation field $\hat{\chi}$. Subfigure (b) also contains 1D profiles (Favre averaged in x, z-directions) of: scalar $\tilde{Z}$, its spatial derivative $\partial\tilde{Z}/\partial y$, and scalar dissipation $\tilde{\chi}$. Here $\chi = 2D\left(\partial Z/\partial x_i\right)^2$), with $D = \lambda/(\rho c_p)$, is representing a measure of the scalar mixing rate at the molecular level. Subfigure (c) also contains 1D profiles of the Favre averaged *x*-velocity $\tilde{u}$, its spatial derivative, and $\tilde{k}$. In subfigure (a), the large-scale structures seen in Fig. 3 become more prominent, as well as sharp scalar gradients, especially near the elongated regions mentioned above. Subfigure (b) clearly shows the oscillating behavior of the large structures. Subfigure (c) shows that the momentum field is more diffused than the scalar field. This is also apparent in the smoothness of the velocity derivative compared with the scalar derivative. The profiles of $\tilde{Z}$ and $\tilde{u}$ also demonstrate the wider spread of the scalar profile compared to the

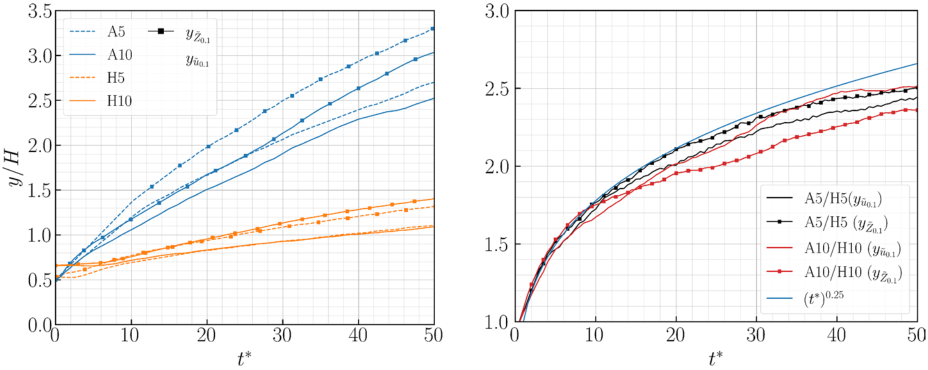

Fig. 4 Evolution of $y_{\tilde{Z}_{0.1}}$ and $y_{\tilde{u}_{0.1}}$ (left), and the ratio of of $y_{\tilde{Z}_{0.1}}$ and $y_{\tilde{u}_{0.1}}$ with respect to composition (right)

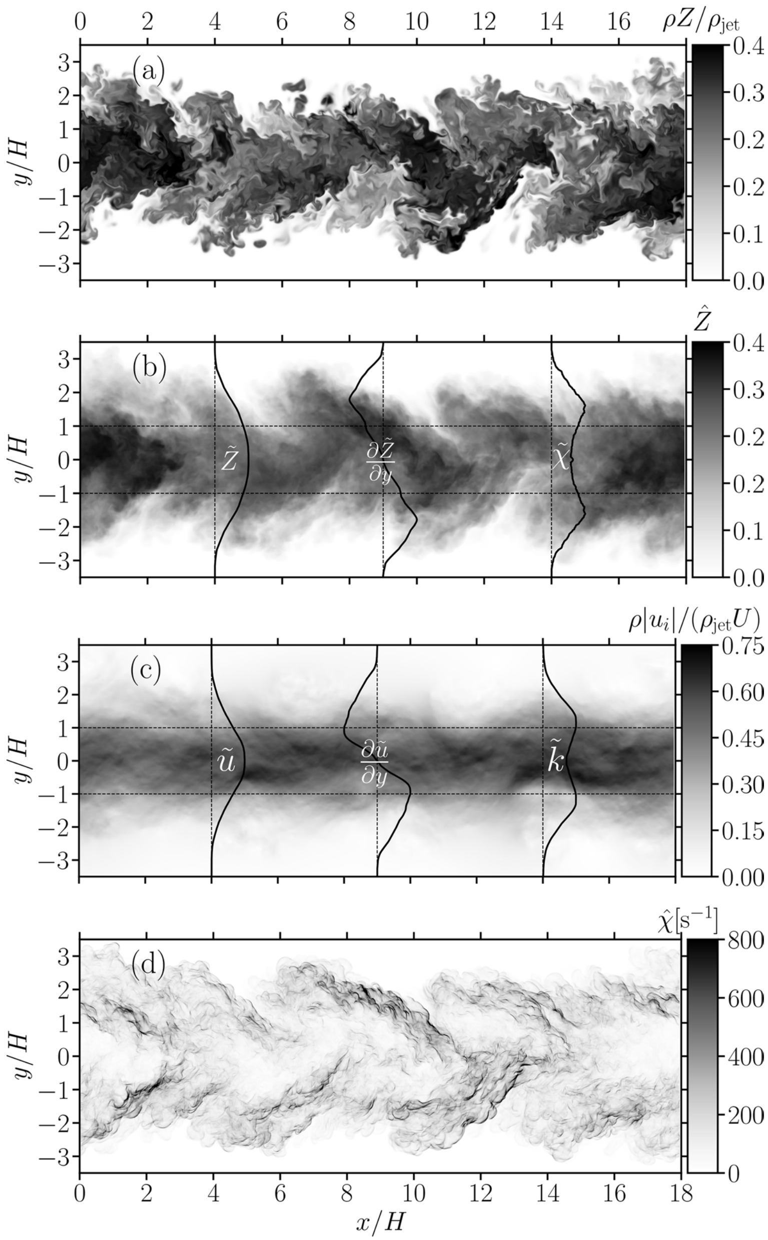

Fig. 5 (**a**) Instantaneous $\rho Z/\rho_{jet}$, (**b**) Favre averaged $\hat{Z}$, (**c**) momentum magnitude and (**d**) Favre averaged scalar dissipation rate, $\breve{\chi}$ for case A10 at $t^* = 40$

profile of momentum, which appears as a shift of position of the peak values of their derivatives, indicating that the scalar flux is stronger than the momentum flux (Eqs. 8, 9). The two quantities contributing to the gradient diffusion model (Eq. 10), the scalar gradient and the turbulence level, here characterized by $\tilde{k}$, have peak values at different positions. The predicted transport peaks where these quantities most favourably combine. The subfigure (d) shows that scalar dissipation rate peaks are found in the elongated regions. The turbulent mixing mechanism is a combination of large vortices engulfing surrounding fluid and diffusion at high scalar gradient locations in the jet core.

Figure 6 presents a visualization of fields for case H10 at $t^* = 40$. In subfigures (a), (c) and (d) the same quantities are displayed as in the corresponding subfigures for case A10 in Fig. 5. Subfigure (b) presents the vorticity computed from the z-averaged velocity fields. Both cases show large structures emerging at each side of the jet, rotating in opposite directions with respect to the plane $y/H = 0$. These structures closely resemble the quasi-two-dimensional idealized structures presented in Bernal and Roshko (1986, Fig. 15). The vorticity plot confirms the existence of counter-rotating vortices on each side of the jet, notwithstanding the existence of smaller structures embedded in the large ones. Focusing on the region near $(x/H, y/H) = (13.5, 0)$ reveals that the large rotating vortex is engulfing high-density fluid (see corresponding region in subfigure (a)) making $\rho|u_i|/(\rho_{\mathrm{jet}}U) > 1$. This same observation applies to each of the elongated regions indicated by straight lines in the subfigure (a). An interesting difference in comparison with case A10 is the presence of sharp gradients in the momentum field in case H10, and the more diffused field in A10. Subfigure (d) shows that case H10 has significantly lower values of $\hat{\chi}$. The explanation is twofold. First, the reduced spreading of the jet due to the large density difference forces the mixing to occur in a smaller relative volume, which will be referred to as 'compactness'. Second, the lower *Le* of H_2 leading to rapid weakening of local scalar gradients. This also explains why the profiles of $\tilde{k}$ and $\tilde{\chi}$ show a single peak in case H10 in contrast with the two peaks in case A10.

Figure 7 shows the streamlines superposed on part of the $\hat{\chi}$ field by using the instantaneous velocity components in x and y-directions. It is revealed that the strongest scalar mixing takes place in the region between the large vortices and the streaks, where the streamlines go from the jet core to the outside.

The appearance of the above described pattern, involving large-scale structures and small scale mixing, as well as the observation of the mean profiles and their relation to the instantaneous phenomena, motivates the deeper analysis via statistics, in order to adequately assess the classical gradient hypotheses. This is done in the following section.

5 Statistical analysis and assessment of models for turbulent fluxes

5.1 Trends in mean profiles

In this section, the density-weighted spatially averaged (in x, z-directions) profiles of the main variables of interest are presented, followed by an assessment of the gradient closure. In Fig. 8, (from the left) the evolution of $\tilde{u}$, $\bar{\rho}\tilde{u}/\rho_{\mathrm{jet}}$ and $\bar{\rho}\tilde{Z}/\rho_{\mathrm{jet}}$ are shown for all cases at $t^* = 10, 30, 50$. On the top row, the Ar cases, and in the bottom row, the H_2 cases. For the Ar cases the profiles of the three considered variables are remarkably similar (especially velocity and momentum). This is not the case for the H_2 cases, which exhibit significant differences of profile shapes between variables. The faster spreading of the Ar jets with respect to the H_2 ones is evident, as well as the faster scalar spreading compared to momentum. Remarkable differences are revealed by comparing the area under the curves. Quantitatively,

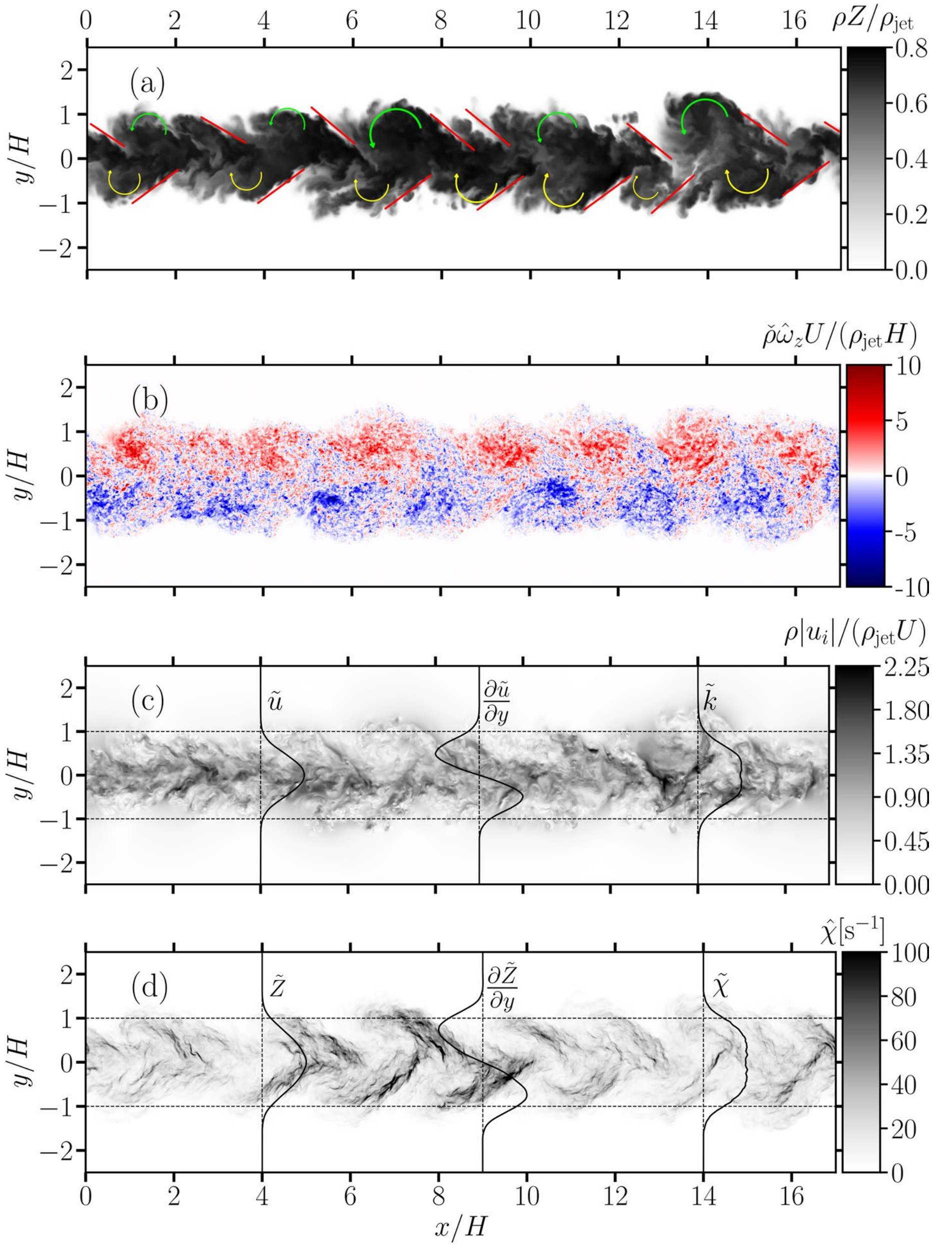

Fig. 6 (**a**) Instantaneous $\rho Z/\rho_{jet}$, (**b**) Favre averaged $\hat{w}_z$, (**c**) momentum magnitude and (**d**) scalar dissipation rate, for case H10 at $t^* = 40$

cases A5 and A10 at $t^* = 50$, show a difference in area under the curves of $\tilde{u}$ vs $\bar{\rho}\tilde{u}/\rho_{\rm jet}$, and $\tilde{Z}$ vs $\bar{\rho}\tilde{Z}/\rho_{\rm jet}$ is about 1–2%. This shows that the compressibility effects are small in an averaged sense, despite the high speed of the jets. The impact of density difference is larger

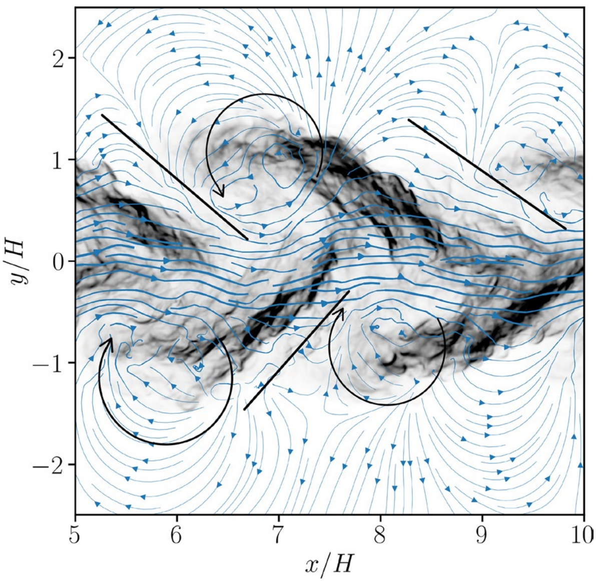

Fig. 7 Streamlines over the scalar dissipation field and drawing indicating the large vortices and elongated regions. The arrows' width is proportional to the local momentum magnitude

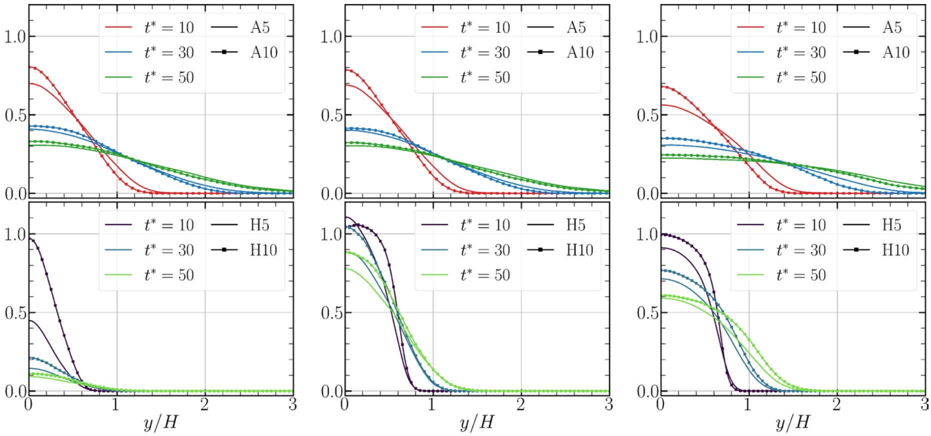

Fig. 8 Top row: argon jets. Bottom row: hydrogen jets. From left to right: mean of velocity ($\tilde{u}/U$), momentum ($\bar{\rho}\tilde{u}/\rho_{\mathrm{jet}}U$), and scalar ($\bar{\rho}\tilde{Z}/\rho_{\mathrm{jet}}$)

in the H_2 cases. The ratio between the area under the curves of $\tilde{u}/U$ vs $\bar{\rho}\tilde{u}/\rho_{\mathrm{jet}}U$ and, $\tilde{Z}$ vs $\bar{\rho}\tilde{Z}/\rho_{\mathrm{jet}}$ is higher by a factor of about 10.

The evolution of density can explain the differences in the behavior of hydrogen and argon jets. Figure 9 shows the evolution of $\bar{\rho}$ and $\bar{\rho}\tilde{v}$, only for H_2 jets as the differences are negligible in the Ar jets. The left figure shows a smooth transition in the density ratio and the right figure shows that in regions where the mean density is increasing, the flow is towards the left and in magnitude has significantly larger value than the flow towards the right in the outer region. This is a sign of the reduced spreading of the jet. The increase in density ratio for $y/H < 0.75$ explains the increase in maximum momentum seen in Fig. 6.

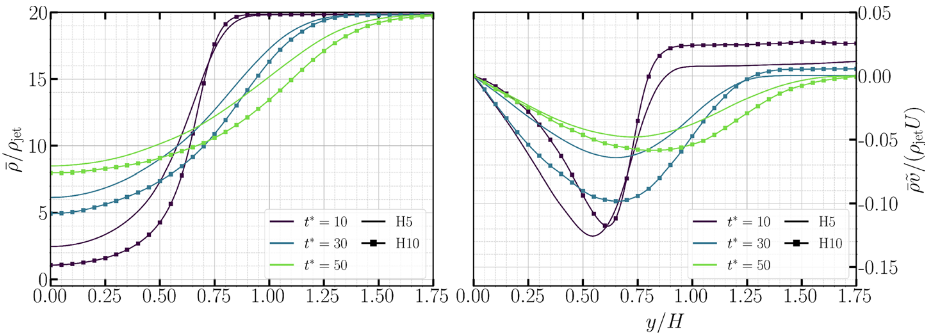

Fig. 9 Mean density and Favre averaged y-velocity for the hydrogen jets

5.2 *A priori* assessment of gradient transport models for turbulent stress and flux

Next, the validity of the gradient hypothesis for turbulent transport of momentum and scalars (Eqs. 8, 9) is assessed a priori by analysis of the DNS results. Results are presented in Fig. 10. Subfigures (a-d) are showing a comparison of both sides of Eqs. 8, 9. The left hand sides (denote 'DNS') are computed directly from local values, and the right hand sides (denoted 'model') are computed from spatial derivatives of the mean variables and using values of $\tilde{k}$, $\tilde{\varepsilon}$, μ_t computed from their definitions (Eqs. 10–13) at fixed standard values $c_\mu = 0.09$ and $\mathrm{Sc}_t = 0.7$. To smoothen the curves of the derivatives, a Savitzky–Golay filter was used with a sample window of 101 points and a third order polynomial. Subfigures (a-d) of Fig. 10 show the second moments normalised with initial jet conditions, for Re=10,000 cases ((a-b) for A10 and (c-d) for H10), at different times. The plotted y/H range has been reduced by half in the H10 case, because the spreading is roughly a factor two smaller. The results for the lower Re were very similar and are not shown.

All cases follow a similar trend. The statistical convergence, characterized by the smoothness of the DNS results, is high in all cases at the first time $t* = 10$, but is decreasing at later times, specially for A10. This may be due to the growth in large structures and dissipation of small structures, leading to a reduced number of independent samples in the averaging procedure, as seen in Sect. 4.

For the cases of Ar jets, the equality of both sides of Eqs. 8, 9 at standard values of c_μ and Sc_t is satisfied remarkably well in the first instance, except for an overshoot at the tip. A common feature in all cases is the higher value of scalar flux compared to momentum flux which can explain the faster scalar spreading seen in Fig. 4. A remarkable deviation is seen in case H10, where the model is overshooting significantly at $t^* = 10$ (figures c-d). At this time value the flow is still very close to the initial condition. When the density increases, the flux also increases, and this is not reproduced by using the standard Sc_t value. This can be quantified by the error in the peak value of the scalar flux profile and the L^2-norm of the difference between the profiles. These are presented in Tables 3, and 4, respectively. The results for cases A5 and H5 are also included. From Table 3, the range of peak errors from first to last time instance is significantly larger in the H_2 cases. In terms of L^2-norm, the errors generally increase in time, except for H10 in the first two instances.

Subfigures (e-f) of Fig. 10 show the values of Sc_t, at which the DNS data satisfy the scalar flux model, Eq. 9, while keeping c_μ at its standard value. It is clear that the required Sc_t

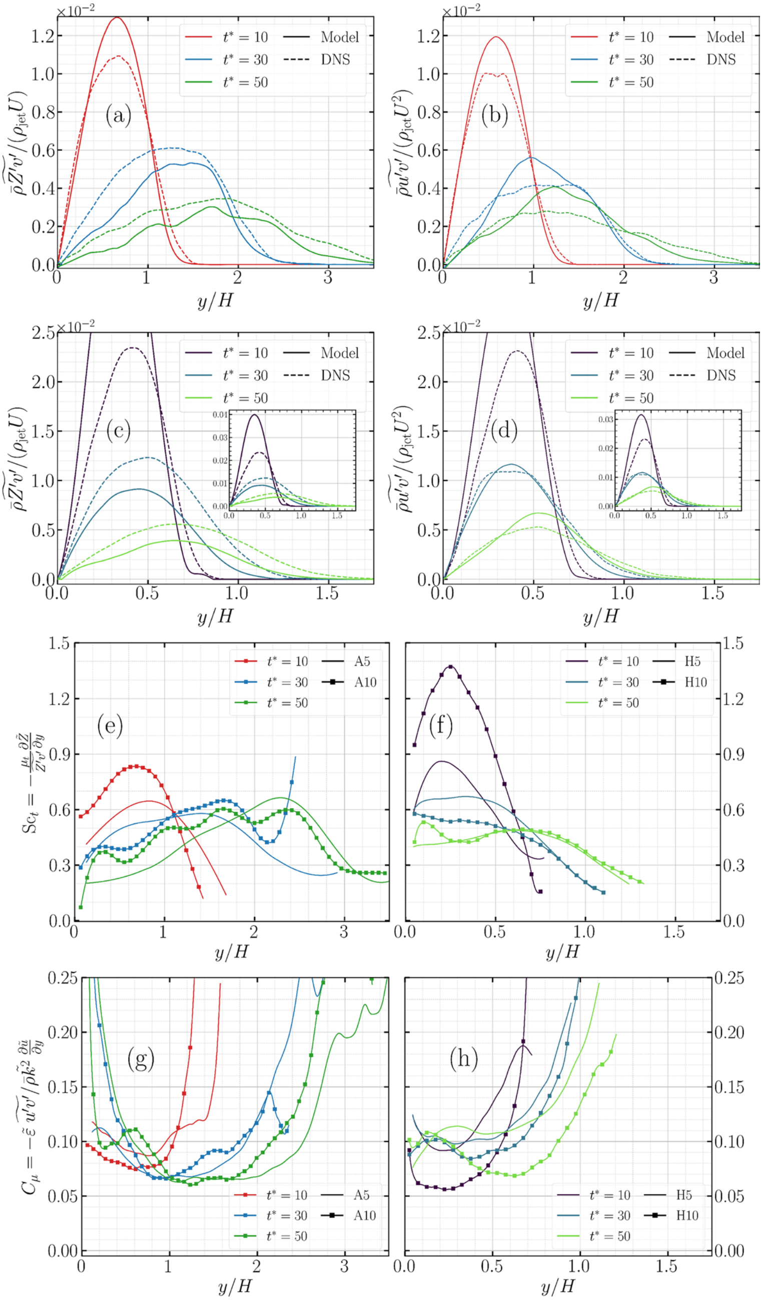

Fig. 10 A priori validation. (**a-d**) comparison of both sides of the gradient diffusion hypothesis Eqs. 8, 9 at standard values of c_μ and Sc_t. Values of Sc_t and c_μ for which the hypothesis Eqs. 8, 9 agrees exactly with the DNS data

Table 3 Error in peak value [%]

t^*/case	A5	A10	H5	H10
10	−5	18	13	70
30	−17	−13	−8	−26
50	−18	−12	−30	−30

Table 4 L^2-norm [%]

t^*/case	A5	A10	H5	H10
10	18	14	19	57
30	30	24	22	33
50	35	30	40	40

is neither constant in space nor constant in time. In case H10 the peak value for Sc_t is found to be 1.4. The range of values decreases with time and relaxes to the range $0.2 - 0.45$. This large difference compared to the standard value 0.7, is attributed to the reduced jet spreading and net influx reported in the previous section. For the Ar jets, the position dependence of Sc_t is also observed, particularly at the first instance, but over time it relaxes to a value in the range $0.3 - 0.65$, showing more variation compared to the H_2 cases. The subfigures (g-h) in Fig. 10 show the values of C_μ, at which the DNS data satisfy the momentum flux model, Eq. 8. It is clear that these values deviate from the standard value 0.09. Values in the range $0.05 - 0.15$ are found for the region where the flux is largest, for both Ar jets and H_2 jets. The next Section shows what the consequences are for the predictive performance of the RANS model.

6 Assessment of RANS and LES predictions

6.1 Validity of gradient diffusion relations

This section presents *a posteriori* validation of the predictions of mean values and second moments by LES and RANS, by comparing them to the DNS results. Because the flow is statistically homogeneous in two directions, it is possible to obtain an ensemble average by spatial averaging of DNS or LES results and compare it to the ensemble average obtained from RANS. Note that for the LES, only the resolved fluctuations are considered to obtain the ensemble averages, not considering the SGS contribution. In RANS, the effective viscosity and diffusivity is used, adding laminar and turbulent contributions. Favre averages are presented to make a fair comparison between the three methods. In Fig. 11 transverse (y-direction) profiles of mean scalar quantities and velocity-scalar cross-correlations, obtained by DNS, LES and RANS are compared. Similar curves for mean velocity and velocity second moments did not provide any extra information as the profiles were very similar, so they are not shown for compactness. Subfigures (a-d) show profiles of normalised mean scalar for cases A5, A10, H5 and H10 at different times. The bottom two rows present the momentum and scalar fluxes for cases A10 and H10, similar to Fig. 10, with the main difference that the scaling is not done with the initial jet density and velocity (ρ_{jet},U), but with the jet-center values $\rho_c, \tilde{u}_c, \tilde{Z}_c$. This allows a better visual assessment, especially for later times.

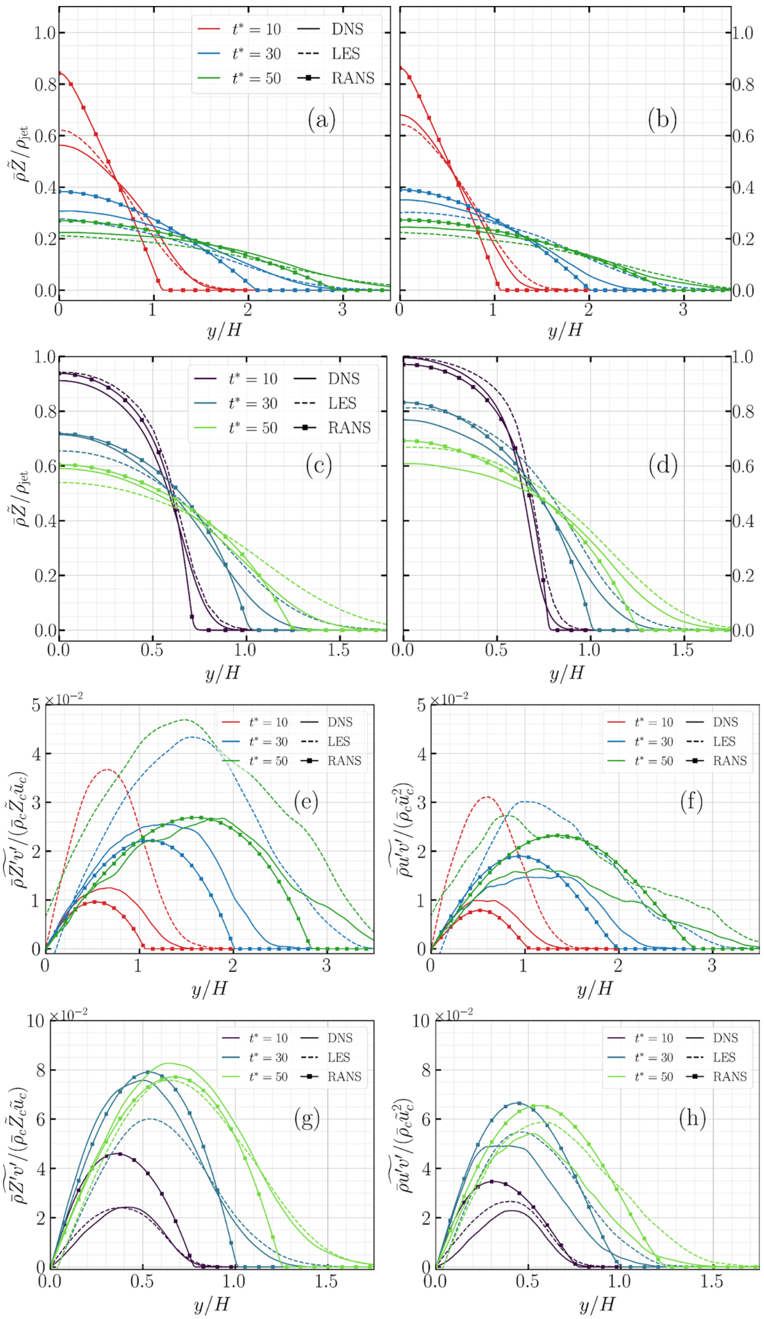

Fig. 11 Comparison of RANS and LES predictions with DNS. (**a**) A5, (**b**) A10, (**c**) H5, (**d**) H10 (**e**) A5, (**f**) A10, (**g**) H5, (**h**) H10

Comparing the mean scalar profiles from DNS and LES for A5 and A10 (a-b) shows excellent agreement of LES with the DNS for A5 in the outer half of the scalar profile. It is slightly under-predicting in the inner half. For case H5, the LES spreads faster and decays faster in the center. For case H10, the opposite is observed. It can be concluded that the mean profiles are qualitatively well predicted by the LES, at both considered *Re*. On the other hand, RANS shows more deviations from DNS. In the Ar jets (e-f), the behavior improves slightly for $Re = 10{,}000$ but the opposite is seen in the H_2 jets (g-h). The most remarkable difference emerges at the edge of the jet, where the RANS prediction shows near zero values too quickly in all cases.

Next, we devote attention to the fluxes. Fig. 11, subfigures (e-h), show profiles of normalised transverse scalar and momentum flux for cases A5, A10, H5 and H10 at different times. These figures help to understand the reasons for agreement and disagreement previously seen. Similar to mean profiles, while LES and DNS behave smoothly decaying profiles at the jet boundary, RANS shows an abrupt transition to zero values. To give a quantitative comparison, Table 5 presents the L^2-norm of the coarse scale method relative to the DNS. LES results improve with increasing *Re* for the later stage, but show significant errors in the early stage. Regarding *Re* dependence, no clear trend is observed for the RANS. The only trend is a reduction in the error with time (except for A10, showing a small increase from the second to third time instance). In summary, the LES and RANS show significantly different quantitative accuracy of flux predictions and the difference is not systematic. An important difference between LES and RANS is in the shape of profiles at the edge of the jet. The reason for this is explored further in the next Sections.

6.2 Analysis of RANS and LES model performance

Because the RANS model shows the largest deviation from the DNS results, first a further analysis of the RANS results is made. To better understand the discrepancies regarding the jet-spreading behavior and properties at the edge of the jet, we compare predictions of k and μ_t, as well as unscaled momentum and scalar fluxes, with DNS results. These profiles are shown in Fig. 12.

It can be seen that the displayed mean variables all are identically zero beyond a certain y-position, in the following called the cut-off. The location is time-dependent but not dependent on the variable. This is a direct consequence of the isotropic eddy viscosity hypothesis. In the mixing layer between a turbulent jet and laminar surroundings, the flow intermittently alternates between laminar and turbulent flow conditions. This is known as external intermittency, in contrast with internal intermittency, which denotes a statistical feature of the energy dissipation rate in any turbulent flow. In most engineering flows, the mean energy dissipation rate provides sufficient information to model turbulent transport and internal intermittency does not need special treatment. In contrast, external intermittency can have a large enough influence to raise the need for model extensions. External intermittency influences the statistics of turbulent transport in a way not described by eddy viscosity

Table 5 L^2 norm of scalar flux difference. Values in percentage with respect to the DNS

Case	A5			A10			H5			H10		
t*	10	30	50	10	30	50	10	30	50	10	30	50
LES	25	20	30	46	46	15	27	21	35	19	30	6
RANS	46	47	26	33	20	23	39	28	13	30	28	22

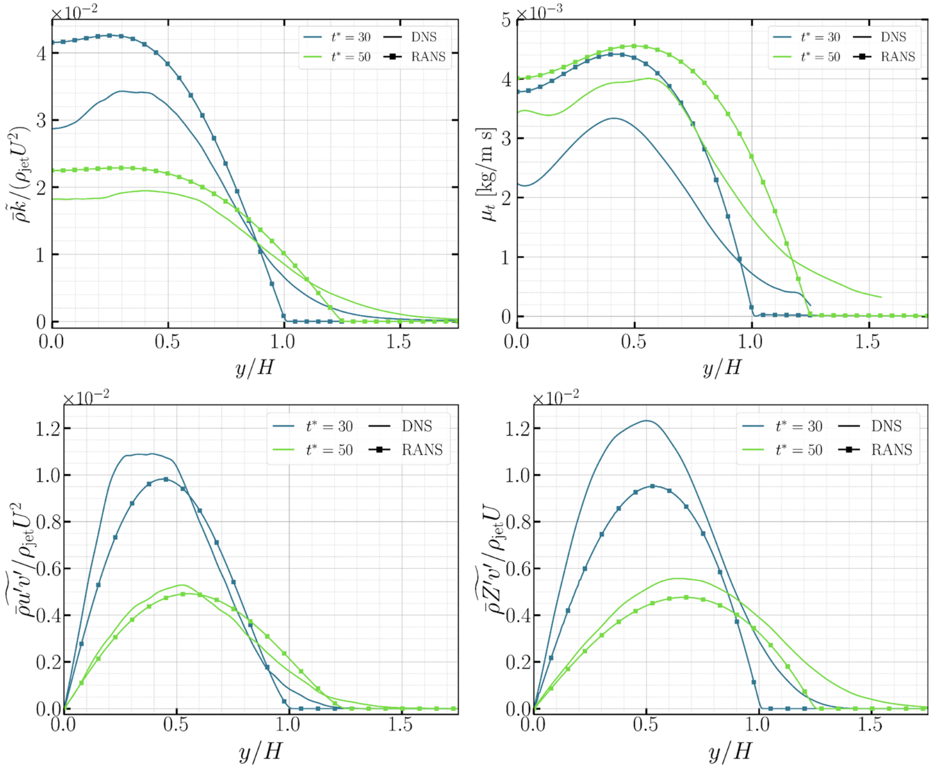

Fig. 12 Validation of key quantities. Top row: turbulent kinetic energy and turbulent viscosity. Bottom row: momentum flux and scalar flux

modeling. Indeed, whenever $k = 0$, also the turbulent diffusivity, the turbulent flux and the production term of k in the k-equation vanish. (Laminar flux has insufficient impact). This is a known limitation of eddy viscosity modeling in describing turbulent mixing near an interface between turbulent and non-turbulent flow (Pope 2005). The efforts to overcome these limitations in RANS and LES have been reviewed by Gilliland et al. (Gilliland et al. 2012) in a study reporting new results for the case of a constant density round jet. For the cases studied here, it is important to note that when turbulent mixing of the scalars is modeled to be controlled by the eddy viscosity, the scalar will not spread beyond the cut-off and the preferential spreading seen in Fig. 4 cannot be captured.

In some cases, the diffusion rate of a scalar can be adequately quantified by adjusting the turbulent Schmidt number, as is often done in practice (Tominaga and Stathopoulos 2007). In the present configuration, this method is not effective. This was tested by using a value of $\mathrm{Sc}_t = 0.4$ for case H10, as suggested from the a priori testing (Fig. 10). The resulting scalar profiles are shown in Fig. 13.

It is clear that the location of the cutoff point is independent of Sc_t, but the profiles become flatter at the top. In other words, the fluxes are larger inside the jet, but abruptness at the boundary remains. Reducing the Sc_t can increase the turbulent diffusion, as expected, but this is only effective in the jet core, where k is non-zero. A lower value of Sc_t gives faster

Fig. 13 Sensitivity of profiles of density weighted scalar to Sc_t

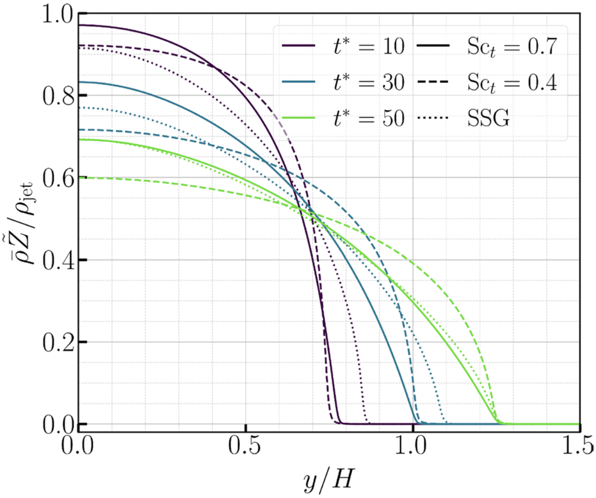

scalar mixing in the interior of the jet, leading to a sharper gradient at the edge without moving the cut-off point.

Proceeding to second-moment closure, i.e. solving transport equations for the Reynolds flux components, does bring some improvements in the predictions of external intermittency problems but cannot eliminate them. This approach predicts the location where k goes to zero further outward from the turbulent region and is found to give better agreement of mean scalar profiles with the DNS result, but the profile still has an abrupt cutoff point. This was confirmed by using the SSG Reynolds stress model in combination with gradient diffusion model for scalars, as implemented in CONVERGE. Making a further step including a differential equation for the turbulent fluxes (full second moment closure) as recommended by Hanjalic and Launder (Hanjalić and Launder 2021), can bring further improvement because in this approach the gradient diffusion assumption is used only at the level of triple correlations. This also enables a more refined modeling of the unclosed pressure-strain-rate correlation in the Reynolds stress equation.

To address the external intermittency problem, specific extensions of RANS modeling have been developed (Cho and Chung 1992). They consider an additional variable (indicator function) to describe the intermittent alternation of turbulent and non-turbulent flow. This can be done both for eddy viscosity models and second moment closure and the proposed models can be divided into two classes, a first class solving transport equations for conditional mean values, (conditional on being in the turbulent flow condition) and a second class where the intermittency effects are explicitly incorporated in the k-ε model (Gilliland et al. 2012). Although these models have been successfully applied in a set of cases, they are less validated and less easy to use with confidence than LES approaches, which offer higher accuracy at higher cost.

In LES the modeling assumptions only concern the subgrid scale and the turbulent scalar flux is sufficiently described by the resolved scales to reach a relatively accurate description of the effect of external intermittency on mean values and fluxes. The phenomena at the turbulent/nonturbulent interface (TNTI) have been reviewed in Ref. (da Silva et al. 2014). Da Silva (da Silva 2009) has analyzed the behavior of some classical SGS models near the interface in a constant density planar temporal jet. The impact of the SGS models on the

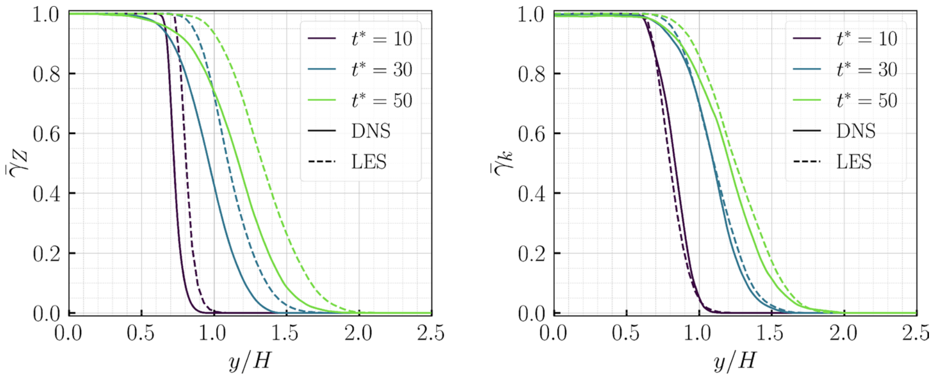

Fig. 14 DNS and LES results for intermittency indicators based on mixture fraction γ_Z and on turbulent kinetic energy γk, at three time instants

predicted shear layer growth was found to be small (about 1%), but accuracy differences between SGS models arise. The results suggest that mixing and reaction rates near the interface should be more affected.

Gilliland et al. (Gilliland et al. 2012) have reported simulations of the TNTI in cylindrical jets using DNS and LES. They used the dynamic model of Germano et al. (Germano 1986) extended with some extra features to enhance numerical stability. Ranga Dinesh et al. (Dinesh et al. 2012) used a similar approach in an LES study of swirl on external intermittency in turbulent jets. The accuracy of the description of external intermittency was validated by comparing values of the 'intermittency value' defined as cumulative probability

$$\gamma_{phi} = \int_{\phi_{\mathrm{th}}}^{\phi_{\mathrm{max}}} P(\psi) d\psi \tag{16}$$

where P denotes the probability density function of the scalar ϕ and ϕ_{th} is a chosen threshold value at the TNTI. (Gilliland et al. 2012) and (Dinesh et al. 2012) considered the mixture fraction $\phi \equiv Z$ to validate how well the LES model describes the effects of external intermittency. Gilliland et al. (Gilliland et al. 2012) have found that LES gives mixture fraction profiles that are too broad compared to equivalent DNS results for a low Reynolds number jet (2400). However, in a high Reynolds number (non-reacting) propane round jet (68000) good agreement with experimental data was found for the mixing field, scalar PDFs and external intermittency. They observed that the results are insensitive to the value of the threshold factor of the intermittency factor in the range [0.01–0.02].

Here we follow the same approach for the case of the variable density temporal mixing layer considering two possible indicators of the interface: γ_Z based on the density-weighted mixture fraction $\phi \equiv \tilde{Z} = \rho Z/\bar{\rho}$ and γ_k based on the resolved turbulent kinetic energy $\phi \equiv k$. The threshold values are $\tilde{Z}_{th} = 0.01$ and $k_{th} = 0.03$. The results obtained for the case H10 are shown in Fig. 14.

Figure 9 shows a comparison of profiles of the intermittency indicators for DNS and LES of the case H10. LES is found to predict the width of the profile of γ_Z too wide compared to the DNS, but γ_k agrees well. The overprediction of the profile width of γ_Z is consistent with that of $\tilde{Z}$ in the tail of the profile shown in Fig. 11d.

We conclude that deficiencies of the LES SGS model in describing intermittency effects do not prevent LES reaching acceptable accuracy of mean profiles and turbulent fluxes. This may be an essential advantage, for example when ignition, taking place at low values of Z, is to be described correctly (Quan Reyes et al. 2024; Mastorakos 2009). But in situations where the ignition phenomena are expected close to the TNTI, model improvements may be needed. For example, in an analysis of DNS results on a turbulent temporally evolving planar non-premixed jet flame of diluted methane fuel in air, Gauding et al. (Gauding et al. 2021) have shown that external intermittency has an impact on higher-order structure functions of turbulence. This information can be incorporated into mixing models via advance modeling of scalar dissipation rate fluctuations in both RANS and LES.

7 Conclusions

DNS of periodic planar jets of $\mathrm{H_2}$ surrounded by Ar were made at $Re = 5000, 10,000$ and contrasted with the case of a jets of Ar into Ar (homogeneous case), to achieve three main goals: First, understand the mixing, momentum and scalar transport. Second, evaluate the classical gradient hypothesis in such configurations considering that the properties of $\mathrm{H_2}$ and Ar largely differ, and there is no guarantee that the classical models would be applicable. Third, evaluate the accuracy of standard RANS and LES approaches against the DNS and suggest improvements. The main conclusions of this study can be summarized as follows:

1. The mixing of $\mathrm{H_2}$ periodic planar jets in Ar strongly deviates from the Ar in Ar case in such that the $\mathrm{H_2}$ jet spreading does not start by up to 10 turn-over times, despite having passed the turbulent transition. This reduced spreading is attributed to the large density ratio between both fluids and the net influx of surrounding mass into the jet. Both effects result in fast scalar mixing. As the fast mixing reduced the large density difference, the spreading of scalar and momentum began to follow a closer trend to that of the homogeneous case after about 40 jet turn-over times.
2. The driving mechanism behind the mixing of the jets resembles that of temporal mixing layers studied earlier in literature, in such that quasi two-dimensional large structures engulf surrounding fluid deep into the jet's core. This engulfment happens through elongate regions formed by the counter-rotation nature of these large vortices. Mixing by diffusion is predominant in these regions. In addition, the cores of the large structures are also aligned with the maximum shear, and the highest turbulent kinetic energy (and vorticity), providing physical arguments to use the mean velocity and scalar, their gradients and the turbulent kinetic energy in closure models.
3. The direct evaluation of the model 'constants' (Sc_t and C_μ) reveals that their local values are not constant in space nor time. For $\mathrm{H_2}$ jets, Sc_t spans one order of magnitude at $t^* = 10$. The variation of the local Sc_t decreases in time to values varying in a small range. This is attributed to the homogenization of the fluids. No such clear 'plateau' is seen for C_μ and it fluctuates more than two-fold. For Ar cases, the local Sc_t has a smaller range, yet three-fold at $t^* = 10$, though it also relaxes to more constant values as time progresses. C_μ has a plateau value of 0.07 lower than the typical 0.09.

4. In the early stage of mixing layer development, spatially averaged profiles predicted by RANS and LES show large deviations from the averages obtained from the DNS (Section 5.1). This can be explained by the fact that the transition to turbulence takes place at scales typical for the Kelvin-Helmholtz instability, that are only resolved by the DNS. The more time progresses though, the three profiles come closer to each other. The profile shape of mean quantities (jet spreading) predicted by the LES is generally in better agreement with DNS than those of RANS. This is due to the fact that the large scales are resolved in LES and not to the better performance of closure models. In fact, a priori assessment of gradient transport models for unresolved fluxes used in RANS and LES (Section 5.2), shows that they have comparable L^2 norm errors.
5. The most prominent difference between the RANS, LES and DNS is in their predictions of the behavior at the jet edge. Standard RANS fails to describe the effects of the turbulent/nonturbulent interface correctly. Not including external intermittency effects, the turbulent kinetic energy profile decays to zero too abruptly, leading to bad prediction of both momentum and scalar transport. This can not be fixed by changing the Sc_t ad hoc. By contrast, LES resolves the interface to sufficient extent to reach good agreement of mean profiles with DNS.
6. The modeling of $\mathrm{H_2}$ mixing in Ar by means of coarse-scale methods must be treated with care, especially if the time of interest is short e.g., $t^* < 30$. At such short times, the standard values of model constants (Sc_t, C_μ) will result in significant errors when using RANS, and LES might not be able to capture the transition to turbulence, and thus the mixing. Furthermore, if the application implies ignition, attention must be placed on the mixing, especially if no sources of turbulent viscosity are present. The wrong prediction of spreading will result in the wrong prediction of ignition location and time.

Acknowledgements This work is part of the project Argon Power Cycle with project number 17868 of the Vici research programme, which is (partly) financed by the Dutch Research Council (NWO). The DNS were performed at the Dutch National Supercomputer, Snellius. We are also grateful to the high-performance computing laboratory (HPC-lab) from Eindhoven University of Technology, for their work in optimizing Disco.

Author contributions D.A.Q.R implemented the boundary conditions in the DNS code, computed the DNS, developed tools for analysing the large data, analysed the data, and contributed to the structure of the study. Also wrote the main manuscript's text and created the figures. N.D. computed the RANS, contributed to the main manuscript's text, provided processed RANS results for the analysis. Significantly contributed to the initial iterations of the study. A.B. computed the LES, provided LES results. D.R. significantly contributed to the analysis and theoretical conceptualization of the study. Provided guidance in the overall process and contributed to the manuscript's text. J.v.O developed the DNS code, significantly contributed to the theoretical conceptualization of the study, helped edit the manuscript's text, and provided guidance in the overall process.

Funding This work is part of the project Argon Power Cycle with project number 17868 of the Vici research programme, which is (partly) financed by the Dutch Research Council (NWO).

Data Availability The data that supports this research is available at the Dutch National Supercomputer's Archive, and may be accessed upon request.

Declarations

Competing interest The authors declare no competing interests.

References

Almagro, A., García-Villalba, M., Flores: O.: a numerical study of a variable-density low-speed turbulent mixing layer. J. Fluid. Mech. **830**, 569–601 (2017)

Ballatore, A., Oijen, J.A.: Pressure-based large-eddy simulation of under-expanded hydrogen jets for engine applications. Int. J. Multiling. Hydrogen Energy **49**, 771–783 (2024)

Ballatore, A., Quan Reyes, D., Bao, H., van Oijen, J.A.: Les-fgm modelling of non-premixed auto-igniting turbulent hydrogen flames including preferential diffusion. Combust Flame **279**, 114270 (2025)

Bastiaans, R.J., Rindt, C.C.M., Nieuwstadt, F.T.M., Van Steenhoven, A.: Direct and large-eddy simulation of the transition of two-and three-dimensional plane plumes in a confined enclosure. Int. J. Heat Mass. Transf. **43**(13), 2375–2393 (2000)

Bastiaans, R.J., van Oijen, J.A., de Goey, L.P.H.: DNS simulations of lean premixed flame kernels with flamelet generated manifolds; an overview. In: ECCOMAS CFD 2006: Proceedings of the European Conference on Computational Fluid Dynamics, Delft University of Technology; European Community on Computational Methods, The Netherlands (2006)

Bernal, L.P., Roshko, A.: Streamwise vortex structure in plane mixing layers. J. Fluid. Mech. **170**, 499–525 (1986)

Boersma, B.J., Brethouwer, G., Nieuwstadt: F.T.M.: a numerical investigation on the effect of the inflow conditions on the self-similar region of a round jet. Phys. Fluids **10**(4), 899–909 (1998)

Browand, F.K.: The structure of the turbulent mixing layer. Physica D. **18**(1–3), 135–148 (1986)

Cho, J., Chung, M.: A k-ϵ-γ equation turbulence model. J. Fluid. Mech. **237**, 301–322 (1992)

Comte-Bellot, G., Corrsin, S.: Simple Eulerian time correlation of full-and narrow-band velocity signals in grid-generated, 'isotropic' turbulence. J. Fluid. Mech. **48**(2), 273–337 (1971)

Coussement, A., Gicquel, O., Caudal, J., Fiorina, B., Degrez, G.: Three-dimensional boundary conditions for numerical simulations of reactive compressible flows with complex thermochemistry. J. Comput. Phys. **231** (2012)

da Silva, C.B.: The behavior of subgrid-scale models near the turbulent/nonturbulent interface in jets. Phys. Fluids **21**(8) (2009)

da Silva, C.B., Hunt, J.C.R., Eames, I., Westerweel, J.: Interfacial layers between regions of different turbulence intensity. Annu Rev Fluid Mech. **46**, 567–590 (2014)

Davidson, T.A.: A simple and accurate method for calculating viscosity of gaseous mixtures. Technical Report RI9456 (1993, US Department of the Interior, Bureau of Mines, USA

Dimotakis, P.E.: The mixing transition in turbulent flows. J Fluid Mech. **409**, 69–98 (2000)

Dinesh, K.K.J.R., Jenkins, K.W., Savill, A.M., Kirkpatrick, M.P.: Swirl effects on external intermittency in turbulent jets. Int J Heat Fluid Flow **33**, 193–206 (2012)

Ern, A., Giovangigli, V.: Fast and accurate multicomponent transport property evaluation. J. Comput. Phys. **120**(1), 105–116 (1995)

Foysi, H., Sarkar, S.: The compressible mixing layer: an les study. Theor. Comput. Fluid Dyn. **24**, 565–588 (2010)

Gatski, T.B., Rumsey, C.L.: In: Launder, B.E., Sandham, N.D.E. (eds.) Linear and Nonlinear Eddy Viscosity Models, pp. 9–46. Cambridge University Press, ??? (2002)

Gauding, M., Bode, M., Denker, D., Brahami, Y., Danaila, L., Varea, E.: On the combined effect of internal and external intermittency in turbulent non-premixed jet flames. In: Proceedings of the Combustion Institute, vol. 38, pp. 2767–2774. (2021)

Germano, M.: A proposal for a redefinition of the turbulent stresses in the filtered Navier-Stokes equations. Phys. Fluids **29**(7), 2323–2324 (1986)

Gilliland, T., Ranga-Dinesh, K.K.J., Fairweather, M., Falle, S.A.E.G., Jenkins, K.W., Savill, A.M.: External intermittency simulation in turbulent round jets. Flow Turbul. Combust. **89**, 385–406 (2012)

Göktolga, M.U., de Goey, L.P.H., van Oijen, J.A.: Modeling curvature effects in turbulent autoigniting non-premixed flames using tabulated chemistry. In: Proceedings of the Combustion Institute, vol. 38(2), 2741–2748. (2021)

Göktolga, M.U., van Oijen, J.A., de Goey, L.P.H.: 3D DNS of mild combustion: a detailed analysis of heat loss effects, preferential diffusion, and flame formation mechanisms. Fuel **159**, 784–795 (2015)

Hanjalić, K., Launder, B.E.: Reassessment of modeling turbulence via reynolds averaging: a review of second-moment transport strategy. Phys. Fluids **33** (2021)

Hill, B.J.: Measurement of local entrainment rate in the initial region of axisymmetric turbulent air jets. J Fluid Mech. **51**(4), 773–779 (1972)

Huang, J.X., Hug, S.N., McMullan, W.A.: Large eddy simulation of the variable density mixing layer. Fluid Dyn. Res. **53**(1) (2021)

Jones, W.P., Launder, B.E.: The prediction of laminarization with a two-equation model of turbulence. Int. J. Heat Mass Transf. **15**(2), 301–314 (1972)
Kim, W.-W., Menon, S.: A new dynamic one-equation subgrid-scale model for large eddy simulations. 33rd aerospace sciences meeting and exhibit. (1995)
Knaepen, B., Debliquy, O., Carati, D.: Direct numerical simulation and large-eddy simulation of a shear-free mixing layer. J Fluid Mech. **514**, 153–172 (2004)
Lange, H.C.: Acoustic upwind for sub- and super-sonic turbulent channel flow at low reynolds number. Int. J. Numer. Methods Fluids **55**(February 2007), 205–223 (2007)
Lele, S.K.: Compact finite difference schemes with spectral-like resolution. J. Comput. Phys. **103**(1), 16–42 (1992)
Lodato, G.: Tridimensional Boundary Conditions for Direct and Large-Eddy Simulation of Turbulent Flows. Sub-Grid Scale Modeling for Near-Wall Region Turbulence. PhD thesis, 2011, Institut National des Sciences Appliqueees de Rouen
Mastorakos, E.: Ignition of turbulent non-premixed flames. Prog. Energy Combust. Sci. **35**(1), 57–97 (2009)
Mathur, S., Tondon, P.K., Saxena, S.C.: Thermal conductivity of binary, ternary and quaternary mixtures of rare gases. Mol Phys. **12**(6), 569–579 (1967)
Moser, R.D., Haering, S.W., Yalla, G.R.: Statistical properties of subgrid-scale turbulence models. Annual review of fluid mechanics downloaded from https://www.annualreviews.org Guest **53**, 255–286 (2021)
Nieuwstadt, F.T.M., Boersma, B.J., Westerweel, J.: Turbulence: introduction to Theory and Applications of Turbulent Flows. Springer, The Netherlands (2016)
Pitsch, H., Peters, N.: A consistent flamelet formulation for non-premixed combustion considering differential diffusion effects. Combust Flame **114**(1–2), 26–40 (1998)
Pitts, W.M.: Reynolds number effects on the mixing behavior of axisymmetric turbulent jets. Exp Fluids **11**(2), 135–141 (1991)
Poinsot, T.J., Lele, S.K.: Boundary conditions for direct simulations of compressible viscous flows. J. Comput. Phys. **101**(1), 104–129 (1992)
Pope, S.B.: Ten Questions concerning the large-eddy simulation of turbulent flows. New J. Phys. **6** (2004)
Pope, S.B.: Turbulent Flows. Cambridge University Press, New York (2005)
Quan Reyes, D.A., Roekaerts, D., Van Oijen, J.: Direct numerical simulation of igniting non-premixed hydrogen combustion for the argon power cycle. In: Proceedings of the Combustion Institute, vol. 40(1-4), 105553. (2024)
Richards, K.J., Senecal, P.K., Pomraning, E.: Converge 3.0. Madison, WI (2021)
Saad, T., Cline, D., Stoll, R., Sutherland, J.C.: Scalable tools for generating synthetic isotropic turbulence with arbitrary spectra. Aiaa J. **55**(1), 327–331 (2017)
Salizzoni, P., Vaux, S., Creyssels, M., Amielh, M., Pietri, L., Anselmet, F.: Turbulent transfer and entrainment in a low-density jet. J Fluid Mech. **968**, 27 (2023)
Salizzoni, P., Vaux, S., Creyssels, M., Craske, J., Van Reeuwijk, M.: Entrainment in variable-density jets. J Fluid Mech. **995**, 11 (2024)
Spalding, D.B.: Turbulent mixing in nonreactive and reactive flows. In: Turbulence Modeling: solved and Unsolved Problems, pp. 85–130. Springer, The Netherlands (1975)
Taguelmimt, N., Danaila, L., Hadjadj, A.: Effects of viscosity variations in temporal mixing layer. Flow Turbul. Combust. **96**, 163–181 (2016)
Tominaga, Y., Stathopoulos, T.: Turbulent Schmidt numbers for CFD analysis with various types of flowfield. Atmos Environ. **41**(37), 8091–8099 (2007)
van Oijen, J.A.: Direct Numerical Simulation of Autoigniting Mixing Layers in MILD Combustion. Center for Turbulence Research, Annual Research Briefs (2011)
Viggiano, B., Dib, T., Ali, N., Mastin, L.G., Cal, R.B., Solovitz, S.A.: Turbulence, entrainment and low-order description of a transitional variable-density jet. J Fluid Mech. **836**, 1009–1049 (2018)
Vreman, A.W., Geurts, B., Kuerten, H.: Large-eddy simulation of turbulent mixing layer. J Fluid Mech. **339**, 357–390 (1997)
Yakhot, V., Orszag, S.A., Thangam, S., Gatski, T.B., Speziale, C.: Development of turbulence models for shear flows by a double expansion technique. Phys. of Fluids A: Fluid Dyn. **4**(7), 1510–1520 (1992)

Authors and Affiliations

Diego A. Quan Reyes[1] · **Nick Diepstraten**[1] · **Alessandro Ballatore**[1] · **Dirk Roekaerts**[2] · **Jeroen van Oijen**[1]

✉ Diego A. Quan Reyes
d.a.quan.reyes@tue.nl

1 Power and Flow, Mechanical Engineering, Eindhoven University of Technology, Eindhoven, The Netherlands

2 Process and Energy, Mechanical Engineering, Delft University of Technology, Delft, The Netherlands